*photonics*

*Article*

# Characterization of Orbital Angular Momentum Beams by Polar Mapping and Fourier Transform

**Ruediger Grunwald * and Martin Bock**

Max-Born-Institute for Nonlinear Optics and Short Pulse Spectroscopy, Max-Born-Strasse 2a, 12489 Berlin, Germany; mbock@mbi-berlin.de

* Correspondence: grunwald@mbi-berlin.de

**Abstract:** The recognition, decoding and tracking of vortex patterns is of increasing importance in many fields, ranging from the astronomical observations of distant galaxies to turbulence phenomena in liquids or gases. Currently, coherent light beams with orbital angular momentum (OAM) are of particular interest for optical communication, metrology, micro-machining or particle manipulation. One common task is to identify characteristic spiral patterns in pixelated intensity maps at real-world signal-to-noise ratios. A recently introduced combination of polar mapping and Fast Fourier Transform (FFT) was extended to novel sampling configurations and applied to the quantitative analysis of the spiral interference patterns of OAM beams. It is demonstrated that specific information on topological parameters in non-uniform arrays of OAM beams can be obtained from significantly distorted and noisy intensity maps by extracting one- or two-dimensional angular frequency spectra from single or concatenated circular cuts in either spatially fixed or scanning mode. The method also enables the evaluation of the quality of beam shaping and optical transmission. Results of proof-of-principle experiments are presented, resolution limits are discussed, and the potential for applications is addressed.

**Keywords:** orbital momentum; polar mapping; Fast Fourier Transform; vortex beams; singular optics; structured light; beam characterization; mode sorting; topological charge; spiral recognition

check for updates

**Citation:** Grunwald, R.; Bock, M. Characterization of Orbital Angular Momentum Beams by Polar Mapping and Fourier Transform. *Photonics* **2024**, *11*, 296. https://doi.org/10.3390/photonics11040296

Received: 14 February 2024
Revised: 13 March 2024
Accepted: 18 March 2024
Published: 25 March 2024



## 1. Introduction

Vortex patterns appear on many scales in nature, from spiral galaxies [1], sunspots [2] hurricanes [3], shells [4] and flower architectures to spiral waves in chemistry [5], double-helix molecules and magnetic skyrmions [6], to mention only a few. Their fast and reliable recognition and tracking at low intensity and/or in the presence of noise is a challenging task. Currently, optical communication systems based on orbital angular momentum (OAM) [7–9] or polarization singularities are of rapidly increasing interest because they exploit additional degrees of freedom and promise robust free-space [10,11] or fiber-based [12,13] data transfer. Such techniques require efficient methods not only for the adaptive generation, encoding, multiplexing and propagation of OAM modes but also for the detection and decoding of two-dimensional optical vortex patterns, even in the presence of turbulence, scattering or absorption in the propagation environment (i.e., atmosphere, ocean, waveguides or fibers). Simulations of the evolution of spiral spectra during propagation in turbulent media suggest the existence of optimum parameters for minimum distortion of data transfer via OAM encoding [14]. The experimental verification of such theoretical predictions, however, requires the appropriate, structurally selective detection techniques.

OAM beams are, in the simplest case, characterized by helical wavefronts twisted around a central singularity [7–9]. In particular, Laguerre–Gauss beams with non-zero topological charges (TC) represent beams of a helical structure. The TC counts the number of intertwined rotated wavefronts and is thus a measure for the OAM density. The direction of wavefront rotation is indicated by the sign of $\ell$. Circular OAM beams with a ring shape can be sorted by their diameter [15], which increases depending on $\ell$. In general, the reliability of the method is rather limited because of the geometrical similarity of the rings. The interference of an OAM beam with a reference wave leads to characteristic spiral patterns which can be unambiguously distinguished [16]. Therefore, the recognition of spiral shapes and counting the number of spiral arms is an alternative approach for tracking, sorting and decoding OAM beams [17,18].

The task of spiral analysis is well known from various areas of research. In fluid dynamics, complex vector fields are described on the basis of Helmholtz–Hodge decomposition, which separates divergence-free and rotation-free components [19,20]. Moreover, vortex cores are located and tracked on the basis of the Navier–Stokes equation [21]. Software for fluid vortex fitting and tracking based on the Lamb–Oseen vortex model for the flow velocity distribution is also available [22].

In astronomy, distant spiral galaxies have to be identified and classified while often detecting only a few photons. The large number of objects requires automated algorithms for spiral arm analysis, e.g., based on random forests [23]. Among the mathematical methods applied to this field, the Fourier transform was one of the most promising approaches [24–26]. The capability of Fourier transform to extract specific spirality information and to distinguish between parabolic, Archimedean and logarithmic spirals in spiral lattices found in selected botanical specimens was successfully demonstrated [27]. Because of the pixelated geometry of matrix detectors and digital phase shapers, studies of discrete spiral analysis are of relevance.

With the fast development of OAM-based optical communication, appropriate mathematical methods for reliably recognizing spiral features have become especially important. To select characteristic rotational features, intensity maps have to be processed via the appropriate transformations. For example, Laguerre–Gaussian transform analysis [28] was applied to optical vortex tracking [29]. With generalized log-polar transformation, high-resolution OAM mode sorting was realized by conformally mapping logarithmic spirals to parallel lines [30,31]. Hough transform algorithms also enable the identification of spiral shapes [32]. Further common techniques for OAM mode sorting are rotational Doppler measurements [33], holography [34–36] or Shack–Hartmann wavefront sensing [37–39].

Recently, the authors proposed a method for determining the TC of OAM beams based on rotational cuts and one-dimensional Fast Fourier Transform (1DFFT) [17]. In this case, background scattering of a Gaussian beam at a spatial light modulator (SLM) was used as a coherent reference wave to generate spiral-shaped interference patterns. A similar mathematical approach based on Fourier transform along circles has been utilized by other authors [40]. The extraction of radial and azimuthal information on modal oscillations was also demonstrated [41]. With extended Fourier methods like Kramers–Kronig interferometry [42], full amplitude and phase retrieval can be obtained with a single-shot spectrum analysis of OAM beams.

Here, we report on two different techniques which represent extensions of previously reported FFT methods along circular cuts [17]. In the following, these methods will be referred to as Fxed Circle Fourier Transform (FCFT) and Scanning Circle Fourier Transform (SCFT), which use static or scanning operation modes, respectively. The applications of both methods to coherent OAM beams shaped by a high-resolution SLM are discussed. The specific capabilities, advantages and disadvantages of the different approaches are also addressed.

## 2. Principle of Fixed Circle and Scanning Circle Fourier Transform Methods

Both methods extract specific information on the spatial modes of structured beams—in particular, the TC of OAM beams—via the Fourier transform of spiral-shaped, two-dimensional intensity maps detected by a matrix camera. Distinct spiral geometries can be obtained by interference of OAM beams with reference beams. For sufficiently extended Gaussian beams, the interference can be approximately described by interference with a plane reference wave. At normal incidence, the resulting intensity pattern has a circular structure with $\ell$ spiral arms [43–46]. The intensity variation with the azimuthal angle $\theta$ can be described for the ideal case [45] by the following theoretical dependence:

$$\left|1 + e^{i\ell\theta}\right|^2 \sim 4\cos^2\left(\frac{i\ell\theta}{2}\right), \tag{1}$$

where $\ell$ denotes the TC. Similar interference patterns are generated with spherical reference waves [45].

For a Fourier analysis of interference maps, different strategies are pursued:

(i) The FCFT method determines the angular frequency spectrum of interference patterns of interest along concentric circles around their center of gravity (COG) and calculates the Fourier transform of this discrete dataset. The COG is typically identical to the position of the singularity. For an optimum performance, the radius of the circle has to be varied until the number of intensity lobes and the corresponding frequency peaks (modes) converge. Thus, the main free parameter is the circle radius $r$.

(ii) The SCFT method extends the FCFT method by additionally scanning the signal map by shifting the centers of the circles and re-calculating the Fourier transform along circles as conducted in FCFT. The variable parameters are the coordinates ($x$,$y$) for the centers of circles and circle radii $r$.

To ensure the comparability of circular cuts of different lengths caused by different radii, equal angular steps are chosen within each set of measurements.

The geometric situations of both methods are depicted schematically in Figure 1. As a realistic example, the spiral-shaped interference pattern of an OAM beam of a TC of $\ell$ = +10 with a coherent, slightly distorted Gaussian background was chosen (Figure 1a).

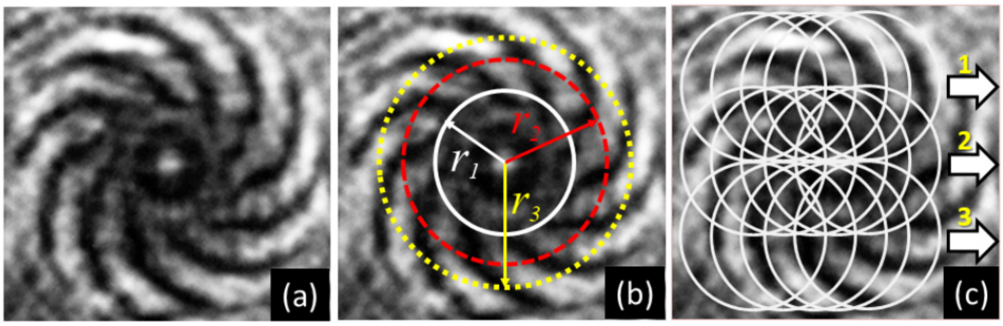


**Figure 1.** Geometrical conditions for OAM beam analysis with Fourier transform (with schematic overlay): (**a**) interference pattern (example: TC $\ell$ = +10); (**b**) Fixed Circle Fourier Transform (FCFT); (**c**) Scanning Circle Fourier Transform (SCFT) mapping a plane of interest. The Fourier transform is performed along a single or multiple circular cuts, respectively. Concentric circles (solid, dashed, dotted) in (**b**) indicate the variation of the radius for three values $r_1$, $r_2$ and $r_3$, respectively. The circles in (**c**) provide a 2D matrix of circular cuts for variable ($x$,$y$)-coordinates (shown for three sequences: 1, 2, 3).

The Fourier transform is performed along concentric circular cuts for FCFT (Figure 1b) or by sampling a detector plane by a matrix of circular cuts around variable ($x$,$y$)-coordinates (SCFT, Figure 1c). The advantage of the SCFT approach is that it can cover more image information, albeit at the cost of an increased number of steps. The maximum radius of the circles determines the maximum possible scan area for full uncut 360° circles. FCFT requires a high accuracy in predefining the singularity position. SCFT works in sequential operation mode and needs to be fast enough to tolerate typical distortions in real-world applications, e.g., due to turbulence. For a reliable identification of the sign of the TC via recognition of the rotational orientation of spiral patterns, two or more circular cuts with different radii are required for each singularity position if the shape distortions can be tolerated. For detection with a pixelated detector, the minimum step widths of radius and position are physically limited by the pixel pitch. In case of SCFT, the usable area for complete circular cuts depends on the radius of the sampling circles. For areas closer to the rim, different strategies can be applied, e.g., by analyzing incomplete circles or adaptively reducing the radius.

SCFT provides more detailed information compared to FCFT and enables one to extract the coordinates of singularities. Therefore, it is particularly interesting for characterizing or decoding arrays of OAM beams and mode sorting. Compared to the quasi stationary analysis with FCFT, the complexity of programming is greater. If FCFT is combined with standard software to determine the COG of spiral patterns (which is available from Shack–Hartmann sensors), the method should also be applicable to the characterization of arrays of OAM beams.

## 3. Experimental Techniques

Single and array-shaped OAM beams were generated by programming helical phase distributions in calibrated grey-scale maps on a 10-megapixel phase-only reflective liquid-crystal-on-silicon (LCoS-) SLM (GAEA, HOLOEYE Photonics, Berlin, Germany) with parallel-aligned liquid crystals which was illuminated by the 5× expanded beam of a linearly polarized Ti:sapphire laser oscillator (center wavelength ~800 nm) [17]. The structured beams were detected by a highly sensitive, near-infrared-enhanced, black-and-white CMOS camera (Thorlabs, Bergkirchen, Germany, DCC 324ONN, 1280 × 1024 pixels, 60 fps). A rotatable polarizer in front of the SLM and additional filters in front of the camera were used to fine-tune the intensity to avoid saturation effects. Because of the interference of the OAM beams with the background signal resulting from the limited fill factor of the SLM, the characteristic spiral patterns appeared as theoretically predicted. Programming of the SLM and the analysis of the image data were performed by two separate computers. The setup is depicted schematically in Figure 2.

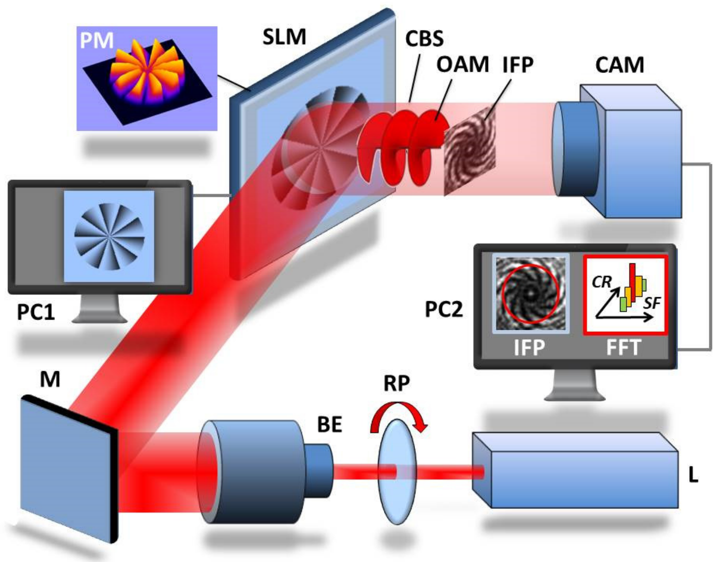


**Figure 2.** Experimental setup for generation and analysis of OAM beams (schematically) (L = laser; BE = beam expander; RP = rotatable broadband polarizer; M = high-reflectance mirror; SLM = spatial light modulator; PC1 = computer for programming SLM; PM = phase map; CBS = coherent background signal; OAM = orbital angular moment beam; IFP = interference pattern; CAM = CMOS camera; PC2 = computer for data processing; FFT = Fast Fourier Transform; CR = cut radius; SF = spatial frequency).

The subsequent image processing steps for the different approaches are presented in the following.

## 4. Results and Discussion

### *4.1. Fixed Circle Fourier Transform*

The first step in FCFT is the rotation of a radial cut of a given length at a given rotational direction around a predefined (or automatically determined) COG in discrete angular steps and the transformation of polar data into a 2D matrix [17]. This data matrix contains the radius (from zero to a maximum value) and the rotation angle as parameters. For a complete rotation cycle over 360°, it visualizes the number of interference fringes, which directly yields information on the TC, its sign and possible radial changes of the slope, indicating radial variations of curvature (analogous to a thread pitch). In Figure 3a,b, two selected measured interference patterns for OAM beams with TC = −5 and TC = +10 are plotted. Corresponding 2D maps from full-circle rotational cuts are compared with each other in Figure 4a,b. Visible distortions were caused by speckles and further interference effects in the optical system.

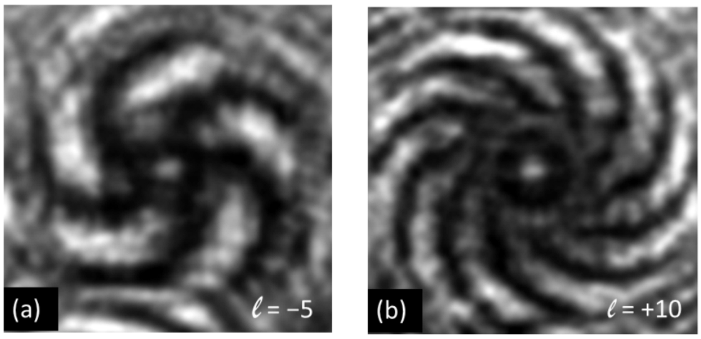


**Figure 3.** Detected free-space interference patterns for sub-beams of an OAM array with (**a**) TC = −5 and (**b**) TC = +10 (analyzed image areas on camera chip: 180 × 172 pixels or 990 × 946 μm$^2$; axial measuring distance $z$ = 3.3 cm, contrast enhanced).

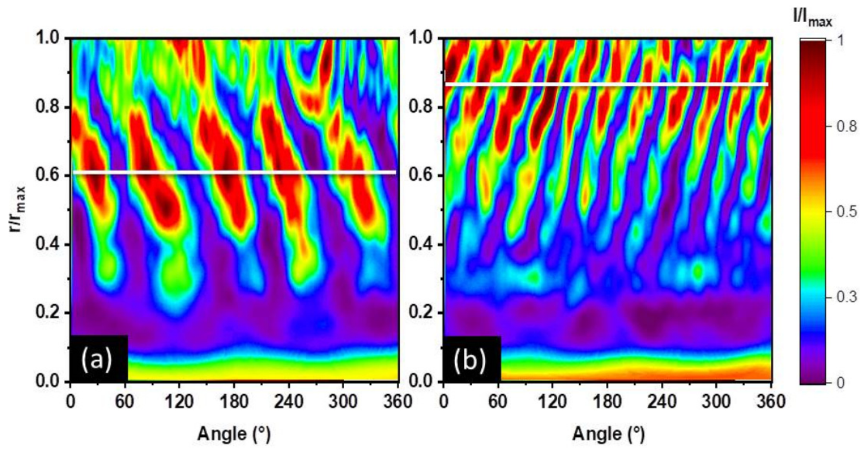


**Figure 4.** Analysis of interference patterns for (**a**) TC = −5 and (**b**) TC = +10 corresponding to Figure 3a,b, respectively. Intensity values along circular cuts at increasing radii were linearly concatenated (360 angular steps, counterclockwise sampling). The maps represent the transformation from polar to Cartesian coordinates.

The Cartesian representation of rotational cuts indicates the TC and sign. Further data processing is enabled by Fourier transform along linear cuts (grey lines in Figure 4a,b) which corresponds to FFT along circles in the unprocessed original data space. The transformed maps show radial variations of the fringe contrast. A selection of appropriate radii can be automated by setting threshold levels for the intensity on the basis of a few uncritical test measurements (if the detector works in non-saturated operation mode) and placing cuts in the center of the encircled areas with suitable contrast. The flexibility in programming the beam configuration and aspect ratio is a specific advantage of shaping with an SLM. Intensity profiles and related spatial frequency amplitudes from the FFT are shown in Figure 5a–d. The different angular frequencies are resolved. Such a measurement can be more difficult if the number of maxima is very small (e.g., for TC < 3). In this case, the FFT for multiple radii has to be analyzed instead of working with only one cut.

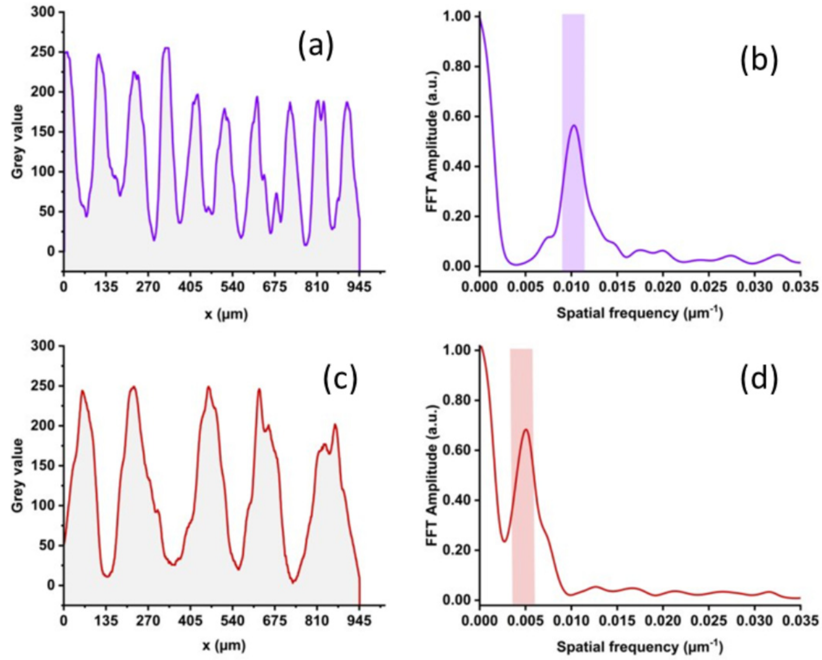


**Figure 5.** Intensity profiles along circular cuts (**a**,**c**) and corresponding spatial frequency spectra (**b**,**d**) for both examples with TC = +10 (violet) and TC = −5 (brown), respectively (slightly smoothed by a B-Spline function, data corresponding to linear cuts in Figure 4a,b).

A variation of the radius of the circle of interest delivers additional information about the radial non-uniformity of the spiral shape, which either results from the limited quality of the reference and structured wavefront or from subtle spatial encoding. The breakdown of the clear spatial frequency signature at increasing radii for TC = −5 is indicated by the FFT spectra in Figure 6.

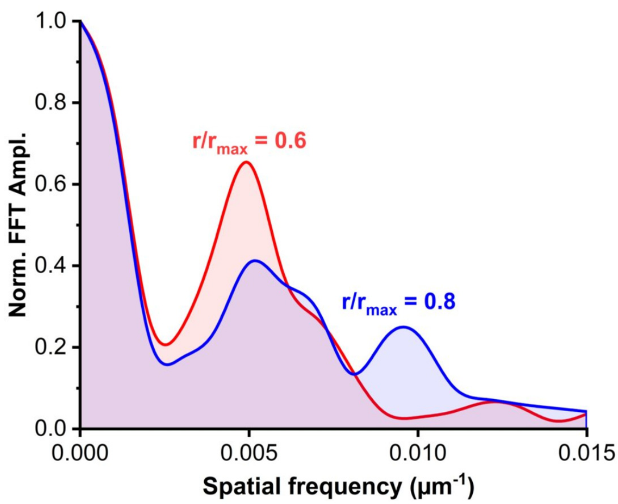


**Figure 6.** Non-uniformity of spiral geometry at TC = −5 indicated by FFT for two concentric circular cuts at different radii. The larger radius (blue curve) corresponds to an imperfect interference pattern containing distortions from neighboring beams, whereas the cut at the smaller radius was nearly undisturbed (red curve).

In this case, the interference pattern was significantly distorted by neighboring sub-beams in an OAM array. A rough resolution criterion can be defined by the ratio of the spatial frequency difference $\Delta\omega(TC) = \omega(TC_i) - \omega(TC_{i+1})$, corresponding to the difference between TC-adjacent sub-beams and the angular frequency shift $\Delta\omega(D)$ due to spatial distortions averaged over the analyzed angular interval. If $\Delta\omega(TC)/\Delta\omega(D) > 1$, relevant spatial frequencies can be separated from the parasitic frequency components.

Another measure for radial non-uniformity is a possible non-linear change in the twist phase with the radius. As Figure 7 shows by comparing the angular positions of fringe centers for an OAM beam with TC = +10, this effect was relatively small for this example.

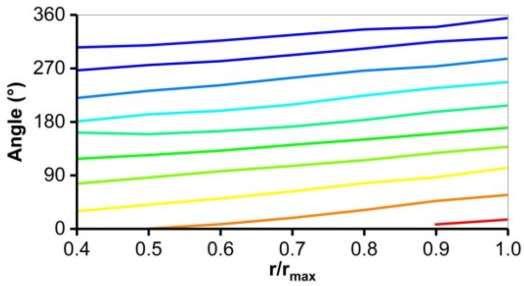


**Figure 7.** Twist uniformity. Changing angular positions of 10 fringe centers of gravity of an OAM beam with TC = +10 as a function of normalized cut radii. Slightly radially dependent distortions are mainly caused by interference effects (the best uniformity is obtained for $r/r_{max}$ between 0.5 and 0.8).

Distortions appear mostly close to the center and rim. On the other hand, with confined software, it could be possible to encrypt information in the non-linearities as well.

More detailed information can be extracted from radial cut maps via two-dimensional Fourier transform (2DFFT), which directly indicates the sense and slope of rotation, as demonstrated in Figure 8a,b. The contour lines were generated by filtering the amplitude maps using appropriate thresholds to suppress noise and parasitic frequencies.

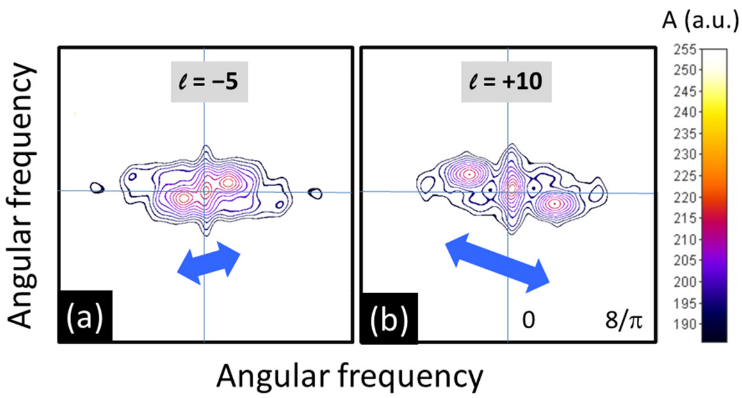


**Figure 8.** Two-dimensional FFT of the radial cut maps for (**a**) TC = −5 and (**b**) TC = +10 as contour plots (for the sake of better visualization, amplitude A was filtered to suppress lower values). The two-step transformation reveals the orientation of the spirals (indicated by the opposite direction of the arrows) as well as the angular frequency which directly provides the TC. (Both 2DFFT maps were calculated with ImageJ, Version 1.53k).

### *4.2. Scanning Circle Fourier Transform*

For the analysis of beam structures with unknown COG positions and/or *multiple* spiral patterns—in particular, for analyzing spatially encoded OAM beam *arrays*—the application of SCFT is preferable. At properly chosen step-widths and ranges of radii, the maps of circular cuts and FFT amplitudes enable one to determine the singularity positions to a good approximation. This will be demonstrated by analyzing an array of

OAM beams of alternating TC (−5, +10) arranged around a central reference needle beam (i.e., a single-lobe Bessel-like beam, as shown in Figure 9.

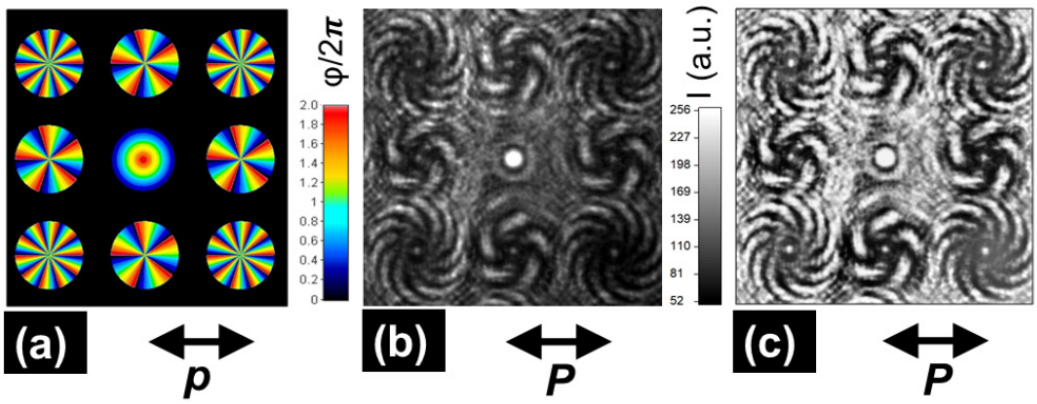


**Figure 9.** Orthogonal array of OAM beams arranged around a central reference beam: (**a**) generating SLM phase map (color code from black to red: phase $\varphi$ from 0 to π for a wavelength of 800 nm); the effective phase is doubled because of reflective operation; (**b**) detected intensity distribution; (**c**) post-processed image (enhanced visibility). Periods in the SLM and detector planes are $p$ and $P$ (FOV on the detector: 1024 × 1024 pixels; pixel size 5.5 × 5.5 μm$^2$).

We note that the phase profile is limited to a maximum value of π because of the reflective operation mode of the SLM. In the experiments, the background intensity signal was typically >50 gray values (in 8 bit mode), i.e., an approximately 20% noise level. Interference effects are caused by the superposition of neighboring sub-beams, filter reflectance, SLM internal grating effects, polarizer, etc., and can be reduced by changing the aspect ratio. Distortions appear mainly at two different scales: (a) speckles with an extension of a few pixels; (b) interference patterns at a scale smaller than the diameter of spiral arms, i.e., typically tens of detector pixels. Thus, the distortions differ by one order of magnitude in spatial extent and also by contrast level. Interference can be filtered out by Fourier filtering and is mostly relevant in regions where adjacent sub-beams overlap.

The combination of scanning and angular sampling is advanatgeous because the robustness against distortions is thereby improved. The minimum required step width related to the resolution of the relevant spiral features has to fulfill the sampling theorem and depends on the characteristic dimensions of the detected spirals. The influence of the displacement of the center of rotating cuts from the real beam center for a selected sub-beam of the array, shown in Figure 9b with TC = +10, is demonstrated in Figures 10 and 11. Concatenated, linearized and normalized circular cuts at horizontal and vertical displacements ($\Delta x$,$\Delta y$) in the detector plane are plotted in Figure 10.

The distributions generated by this specific transformation via circular cuts exhibit characteristic features. In a second step, these intensity maps were analyzed via 2DFFT. The amplitude maps of corresponding angular frequencies $\Omega = 1/\varphi$ for the same dataset (Figure 11) enable one to extract the parameters for classification and sorting, e.g., on the basis of adapted contrast and fragmentation operators.

In general, the analysis of extended spiral-shaped arrays is a complex optimization problem and requires sophisticated image recognition techniques. The results of the scanning circle analysis of the beam array structure shown in Figure 9b are presented in Figure 12a–d for four parts of the sampled area, each covering 7 × 8 center positions.

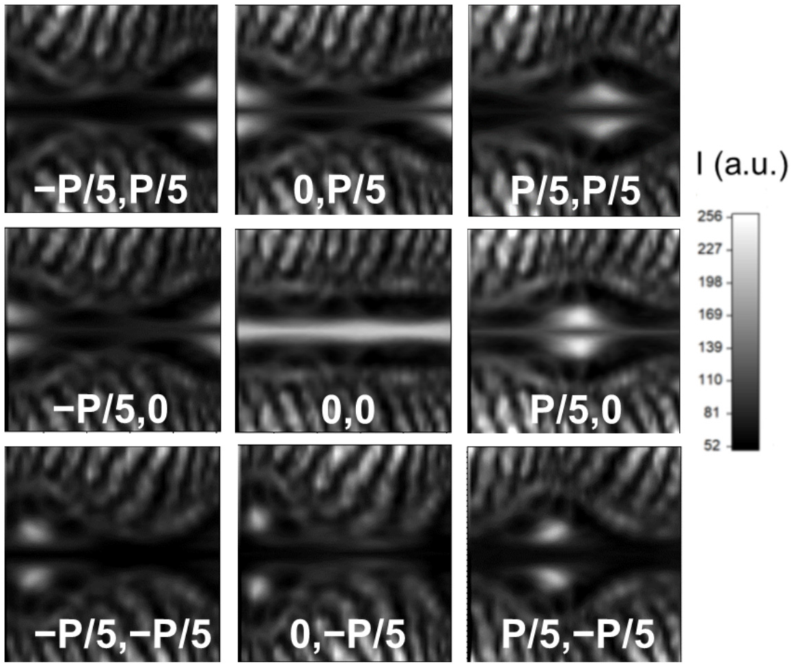


**Figure 10.** Concatenated, linearized and normalized circular cuts for a sub-beam of TC = +10 at horizontal and vertical displacements ($\Delta x$,$\Delta y$) in steps of $P/5$. The numbers in the Figures indicate the center positions of cut circles ($P$ = 340 pixels = period at the detector plane; 50 cuts, horizontal axes; rotation angle from 0 to 2π vertical axes; radii of cuts from $r_{min}$ = 0 to $r_{max}$ = 90 pixels corresponding to 0.265 $P$; central image: position with zero displacement).

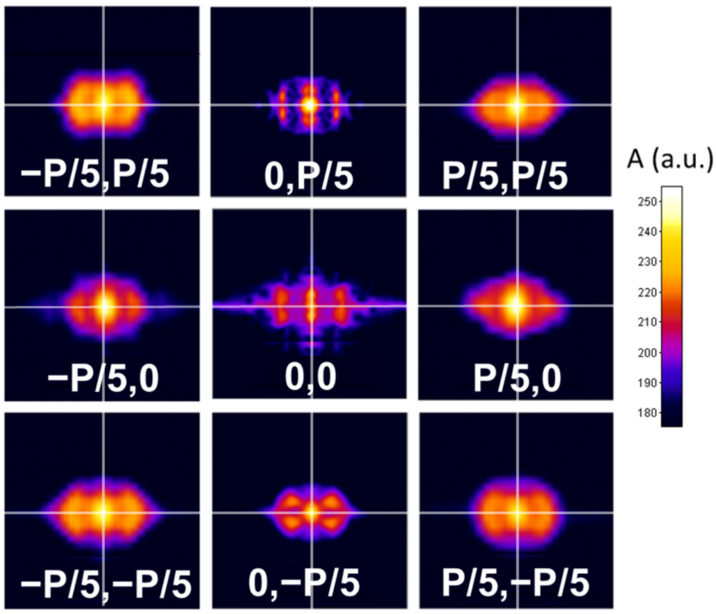


**Figure 11.** 2DFFT amplitudes corresponding to the dataset used for Figure 10. The angular frequency axes cover a range between 0 (centers) and 32 × (1/2π).

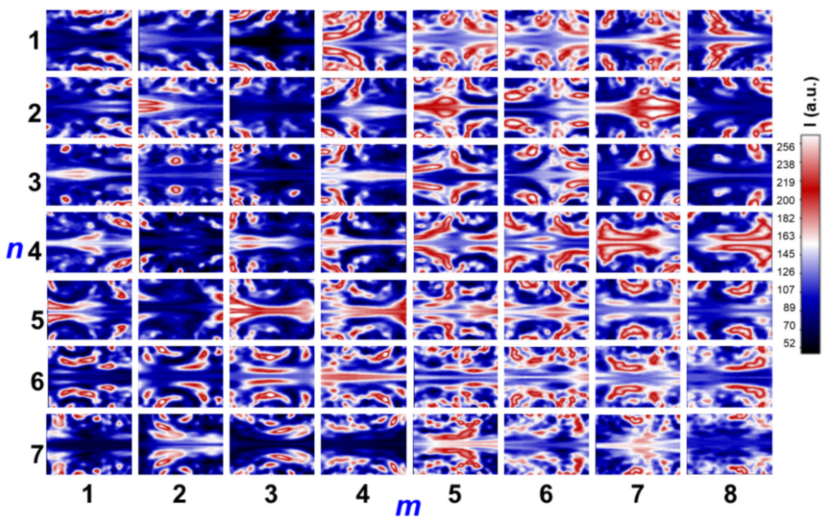


(**a**)

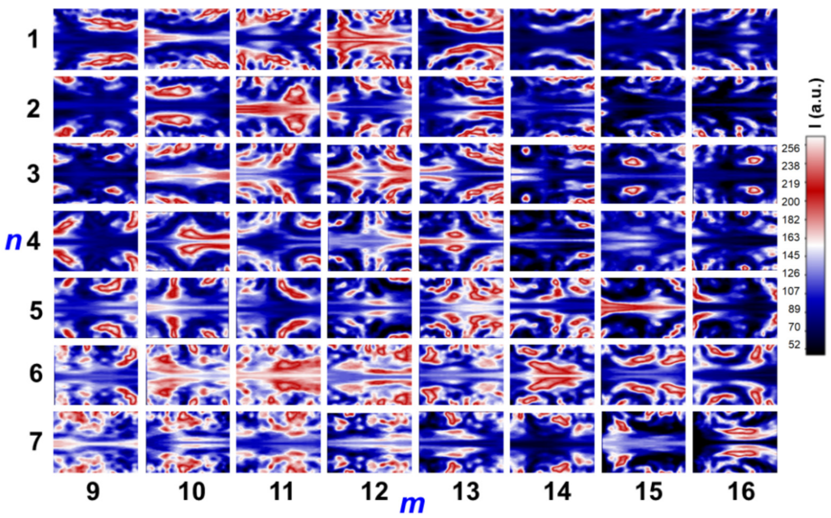


(**b**)

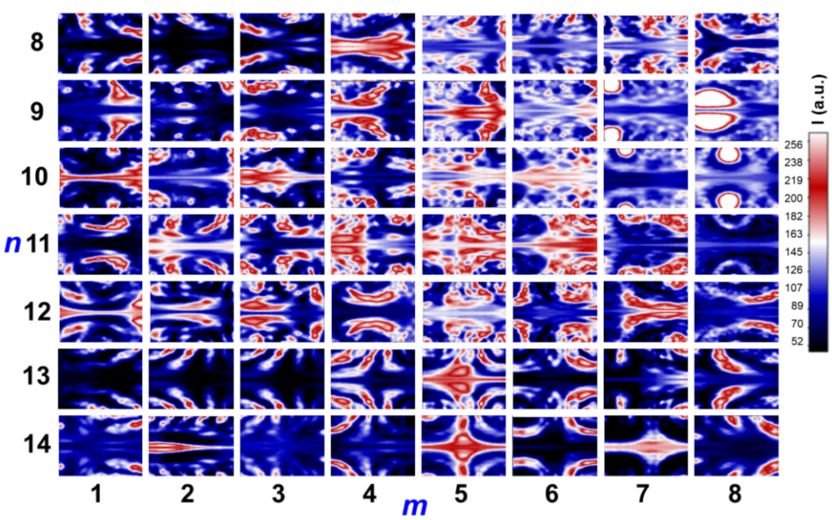


(**c**)

**Figure 12.** *Cont*.

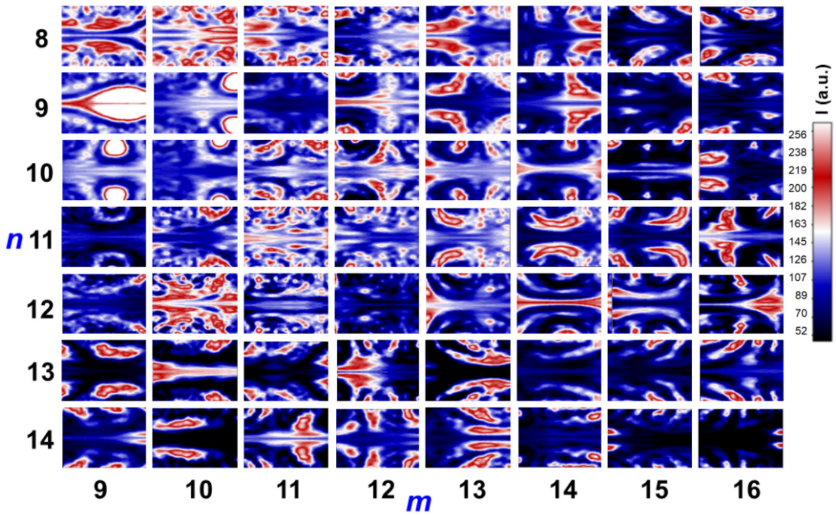


(**d**)

**Figure 12. SCFT experiment:** (**a**) First quarter of a map of local polar plots for the OAM beam array in Figure 9b (upper left part, mirrored half-circle cuts, horizontal and vertical axes; rotation angle from 0 to $\pi$ and cut radii from 0 to 100 pixels, respectively). The image (total size: 1024 $\times$ 1024 pixels) was partially sampled in steps of 50 pixels, from starting point (91,90) in a coordinate system with origin (0,0) at the upper left corner (number of rotation centers: 14 $\times$ 16 = 224) (to enhance the visibility of the interference patterns, blue-red coloration was applied (color code: Union Jack, ImageJ LUT)). (**b**) Second quarter of the scanned area of the OAM beam array (upper right part). (**c**) Third quarter of the scanned area of the OAM beam array (lower left part). (**d**) Fourth quarter of the scanned area of the OAM beam array (lower right part).

To enhance the visibility of the changing interference patterns along the scan, the pictures were colored using Union Jack standard color code (ImageJ, see the color bars). The original gray-level data of the polar plots are not shown for this intermediate state of the SCFT analysis but were the basis for further FFT analysis. To minimize computing effort, the polar transformation was performed in spatial sampling steps of about $r/P = 0.16$ at 50 cut radii between 0 and a maximum radius of 100 pixels or $r/P = 0.32$. In contrast to Figure 10, the images correspond to mirrored half circles (rotation angle interval $\Delta\theta$ from 0 to $\pi$) to facilitate a visual assessment. The resulting matrix of concatenated cuts looks very complex but already indicates the positions of the OAM beams. By subsequent 1DFFT or 2DFFT, the rearranged intensity maps can further be processed. For the sake of simplicity, we selected cuts at a radial distance of 4/5 of the maximum cut radius (corresponding to horizontal lines in Figure 12a–d) and calculated related angular frequency amplitudes by FFT for all 224 positions. By filtering out theoretically expected frequencies for TC = 10 and TC = $-5$, a spatial map of the array topology was obtained (Figure 13).

In this proof-of-principle experiment, the resolution was limited by the relatively large step width. In a fully automated procedure, resolution and recognition accuracy could be significantly improved. Furthermore, the sign of the local TC could also be extracted as shown for the FCFT method. In general, the direct visual representation of three- or four-dimensional FFT data is not trivial. One strategy could be the introduction of statistical meta-moments, as recently demonstrated for the spatiospectral analysis of ultrashort-pulsed OAM beams [47]. Such algorithms for an appropriate quantitative characterization are currently still under development. The high complexity of extended polar and SCFT maps promises to be an interesting field for the application of machine learning algorithms.

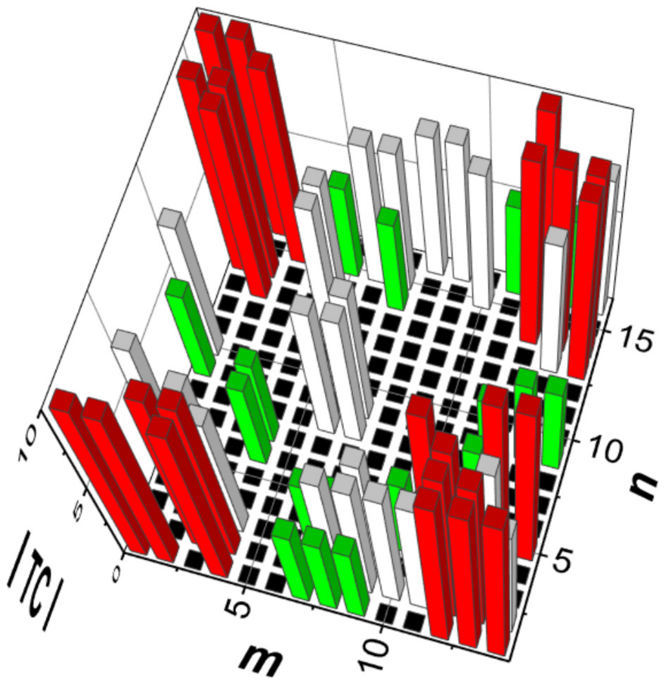


**Figure 13.** Map of absolute values of TC corresponding to array data from Figure 12a–d reconstructed via SCFT on the basis of single cuts through the polar plots and 1DFFT for each COG coordinate. The arrangement of alternating sub-beams with |TC| = 10 (red bars) and |TC| = 5 (green bars) is clearly indicated. White bars stand for ambiguous frequency spectra (for convenience only, this was set to TC = 7.5).

## 5. Conclusions

In summary, different approaches for spatially analyzing OAM beams based on a combination of conformal mapping [48] and Fourier transform procedures are reported, which essentially extend a previous proposal by the authors [17]. Fixed Circle Fourier Transform (FCFT) performs a polar transformation via circular cuts at rotation angles $\theta$ and variable radii $r$, providing two-dimensional ($r$,$\theta$) maps which are further processed by one- or two-dimensional FFT. Rotational orientation and angular frequency spectrum can be extracted directly via 2DFFT.

Compared to single-shot-capable FCFT, Scanning Circle Fourier Transform (SCFT) spatially scans the interference patterns. This not only enables one to sort OAM modes, to identify the TC and to determine the rotational orientation of single or multiple OAM beams; one can also read out further encoded spatial information, e.g., adjustment markings for centering and scaling. Non-linearities, i.e., deviations from the ideal curvature of interference spirals, can be exploited to encrypt additional information. Because of scanning the complete intensity map, image processing does not require a priori knowledge of COG and is not limited to rotational symmetric mode patterns. The sequential SCFT procedure is more time-consuming but extends the field of applications to structured beams of even higher complexity. From our results, it is evident that scanning procedures have the potential to improve recognizability because of multiple sampling coordinates (redundancy). The quantitative recognition rate, however, depends strongly on all system parameters. SCFT applications could be the characterization and decoding of OAM beam arrays, Talbot experiments, or wavefront sensing with OAM encoded beams [17].

Image-based Fourier techniques surpass the limited spatial resolution of wavefront sensors but could be completed by the capability to directly determine temporal wavefront autocorrelation in advanced configurations [39,49]. Digital–holographic single-shot detection methods [50], which also work with reference beams, could be combined with our approaches. It has to be expected that machine learning algorithms will contribute to the development of improved analysis software and advanced data visualization. We also note that adaptive techniques [51] and the combination of the Gerchberg–Saxton approach with neural network recognition [52] are further promising options. In a very recent publication of Li et al., fast extraction of spiral spectra from the coherence-orbital angular momentum (COAM) matrix of partially coherent beams was performed on the basis of off-axis holography and Cartesian–polar coordinate transformation [53].

Finally, we emphasize that the application field of the developed techniques is not primarily the well-established optical communication with OAM beams at an extremely high data transmission speed, which has already reached high rates and excellent recognition performance [54,55].

In general, the combination of polar mapping and FFT analysis in fixed or scanning mode enables one to efficiently characterize and recognize beam arrays or more complex patterns which are of relevance in optical metrology, wavefront sensing and beam tracking (compare ref. [17]). There is a large potential in a range of applications where individually encoded sub-beams of beam arrays have to be identified and adapted, or where self-imaging configurations transfer spatiotemporal information on laser–matter interaction to a distant detector. The measuring principles enable one to analyze and select characteristic features of mode structures, interference patterns or astronomical images and to evaluate the quality of beam shaping and optical transmission systems. Other applications may be possible in theoretical physics, e.g., for the analysis of quantum information entropy in multiple quantum well systems [56,57], for the description of partial quantumness by the Wigner function [58] or similar topics.

At the current stage, our calculations were performed on the basis of modular software building blocks. Integration of the software into a single block and extension to AI algorithms will be an important task for the future.

**Author Contributions:** Conceptualization and methodology, R.G. and M.B., experiments R.G.; software M.B.; data analysis, R.G. and M.B., writing—original draft preparation, R.G.; writing—review and editing, R.G. and M.B.; visualization, R.G. and M.B.; project administration and funding acquisition, R.G. The authors declare that no support by AI was used. All authors have read and agreed to the published version of the manuscript.

**Funding:** This research was funded in parts by Deutsche Forschungsgemeinschaft (DFG), project MAXWELL III, grant number GR1782/16-2.

**Institutional Review Board Statement:** Not applicable.

**Informed Consent Statement:** Not applicable.

**Data Availability Statement:** Data are contained within the article.

**Acknowledgments:** Experimental resources including lab space and laser systems were kindly provided by Elsaesser and Erik Nibbering (MBI). The authors thank Jahns (FernUniversity, Hagen) for stimulating discussions. Mathias Jurke (MBI) was involved in previous experiments on the digital generation of OAM patterns. The authors thank Enda McGlynn for comments and critical review of the manuscript.

**Conflicts of Interest:** The authors declare no conflicts of interest.

## References

1. Hubble, E.P. *The Realm of Nebulae, Mrs. Hepsa Ely Silliman Memorial Lectures, 25*; Yale University Press: New Haven, CT, USA, 1936; pp. 124–151.
2. Kang, J.; Chae, J.; Nakariakov, V.M.; Cho, K.; Kwak, H.; Lee, K. The physical nature of spiral wave patterns in sunspots. *Astrophys. J. Lett.* **2019**, *877*, L9. [CrossRef]
3. Montgomery, M.T.; Kallenbach, R.J. A theory for vortex Rossby-waves and its application to spiral bands and intensity changes in hurricanes, Q.J.R. *Meteorol. Soc.* **1997**, *123*, 435–465. [CrossRef]
4. Clark, J.V.; Aldridge, A.E.; Reolid, M.; Endo, K.; Pérez-Huerta, A. Application of shell spiral deviation methodology to fossil brachiopods: Implications for obtaining specimen ontogenetic ages. *Palaeontol. Electron.* **2015**, *18*, 1–39. [CrossRef]
5. Epstein, I.R. Spiral waves in chemistry and biology. *Science* **1991**, *252*, 67. [CrossRef]

6. Everschor-Sitte, K.; Masell, J.; Reeve, R.M.; Kläui, M. Perspective: Magnetic skyrmions–overview of recent progress in an active research field. *J. Appl. Phys.* **2018**, *124*, 240901. [CrossRef]
7. Allen, L.; Beijersbergen, M.W.; Spreeuw, R.J.C.; Woerdman, J.P. Orbital angular-momentum of light and the transformation of Laguerre-Gaussian laser modes. *Phys. Rev. A* **1992**, *45*, 8185–8189. [CrossRef]
8. Yao, A.M.; Padgett, M.J. Orbital angular momentum: Origins, behavior and applications. *Adv. Opt. Photon.* **2011**, *3*, 161–204. [CrossRef]
9. Padgett, M.; Courtial, J.; Allen, L. Advances in optical angular momentum. *Phys. Today* **2004**, *57*, 35–40. [CrossRef]
10. Willner, A.E.; Huang, H.; Yan, Y.; Ren, Y.; Ahmed, N.; Xie, G.; Bao, C.; Li, L.; Cao, Y.; Zhao, Z.; et al. Optical communications using orbital angular momentum beams. *Adv. Opt. Photonics* **2015**, *7*, 66–106. [CrossRef]
11. Wang, J.; Liu, J.; Zhao, Y.; Du, J.; Long, Z. Orbital angular momentum and beyond in free-space optical communications. *Nanophotonics* **2022**, *11*, 645–680. [CrossRef]
12. Yue, Y.; Yan, Y.; Ahmed, N.; Yang, J.Y.; Zhang, L.; Ren, Y.; Huang, H.; Birnbaum, K.M.; Erkmen, B.I.; Dolinar, S.; et al. Mode properties and propagation effects of optical orbital angular momentum (OAM) modes in a ring fiber. *IEEE Photonics J.* **2012**, *4*, 535–543.
13. Ma, M.; Lian, Y.; Lu, Z. Generation, Transmission and Application of orbital angular momentum in optical fiber: A review. *Front. Phys.* **2021**, *9*, 773505. [CrossRef]
14. Zeng, J.; Liu, X.; Zhao, C.; Wang, F.; Gbur, G.; Cai, Y. Spiral spectrum of a Laguerre-Gaussian beam propagating in anisotropic non-Kolmogorov turbulent atmosphere along horizontal path. *Opt. Express* **2019**, *27*, 25342–25355. [CrossRef]
15. Harm, W.; Bernet, S.; Ritsch-Marte, M.; Harder, I.; Lindlein, N. Adjustable diffractive spiral phase plates. *Opt. Express* **2015**, *23*, 413–421. [CrossRef] [PubMed]
16. Vickers, J.; Burch, M.; Vyas, R.; Singh, S. Phase and interference properties of optical vortex beams. *J. Opt. Soc. Am. A* **2008**, *25*, 823–827. [CrossRef] [PubMed]
17. Grunwald, R.; Jurke, M.; Liebmann, M.; Bock, M. Orbital angular momentum encoded beam tracking and wavefront sensing. *IEEE J. Light. Technol.* **2023**, *41*, 2017–2024. [CrossRef]
18. Huang, H.; Ren, Y.; Yan, Y.; Ahmed, N.; Yue, Y.; Bozovich, A.; Erkmen, B.I.; Birnbaum, K.; Dolinar, S.; Tur, M.; et al. Phase-shift interference-based wavefront characterization for orbital angular momentum modes. *Opt. Lett.* **2013**, *38*, 2348–2350. [CrossRef]
19. Bhatia, H.; Norgard, G.; Pascucci, V.; Bremener, P.-T. The Helmholtz-Hodge decomposition—A survey. *IEEE Transact. Visual. Comp. Graph.* **2013**, *19*, 1386–1404. [CrossRef]
20. Haufe, D.; Gürtler, J.; Schulz, A.; Bake, F.; Enghardt, L.; Czarske, J. Aeroacoustic analysis using natural Helmholtz-Hodge decomposition. *J. Sens. Sens. Syst.* **2018**, *7*, 113–122. [CrossRef]
21. Finn, L.I.; Boghosian, B.M.; Kottke, C.N. Vortex core identification in viscous hydrodynamics. *Philos. Trans. A Math. Phys. Eng. Sci.* **2005**, *363*, 1937–1948. [CrossRef]
22. Lindner, G.; Devaux, Y.; Miskovic, S. VortexFitting: A post-processing fluid mechanics tool for vortex identification. *SoftwareX* **2020**, *12*, 100604. [CrossRef]
23. Silva, P.; Cao, L.T.; Hayes, W.B. SpArcFiRe: Enhancing spiral galaxy recognition using arm analysis and random forests. *Galaxies* **2018**, *695*, 95. [CrossRef]
24. Puerari, I.; Dottori, H.A. Fourier analysis of structure in spiral galaxies. *Astron. Astrophys. Suppl. Ser.* **1992**, *93*, 469–493.
25. Puerari, I.; Dottori, H.A. A morphological method to determine corotation radii in spiral galaxies. *Astrophys. J.* **1997**, *476*, L73–L75. [CrossRef]
26. Davis, B.L.; Berrier, J.C.; Shields, D.W.; Kennefick, J.; Kennefick, D.; Seigar, M.S.; Lacy, C.H.S.; Puerari, I. Measurement of galactic logarithmic spiral arm pitch angle using two-dimensional Fast Fourier Transform decomposition. *Astrophys. J. Suppl. Ser.* **2012**, *199*, 33. [CrossRef]
27. Xudong, F.; Bursill, L.A.; Lin, P.J. Fourier transforms and structural analysis of spiral lattices. *Int. J. Mod. Phys. B* **1988**, *2*, 131–146.
28. Wei, D.; Ma, J.; Wang, T.; Xu, C.; Zhu, S.; Xiao, M.; Zhang, Y. Laguerre-Gaussian transform for rotating image processing. *Opt. Express* **2020**, *28*, 26898–26907. [CrossRef] [PubMed]
29. Szatkowski, M.; Burnecka, E.; Dyła, H.; Masajada, J. Optical vortex tracking algorithm based on the Laguerre-Gaussian transform. *Opt. Express* **2022**, *10*, 17451–17464. [CrossRef] [PubMed]
30. Wen, Y.; Chremmos, I.; Chen, Y.; Zhu, J.; Zhang, J.; Zhang, Y.; Yu, S. Spiral transformation for high-resolution and efficient sorting of optical vortex modes. *Phys. Rev. Lett.* **2018**, *120*, 193904. [CrossRef] [PubMed]
31. Berkhout, C.G.; Lavery, M.P.J.; Courtial, J.; Beijersbergen, M.W.; Padgett, M.W. Efficient Sorting of Orbital Angular Momentum States of Light. *Phys. Rev. Lett.* **2010**, *105*, 153601. [CrossRef]
32. Torrente, M.-L.; Biasotti, S.; Falcidien, B. Recognition of feature curves on 3D shapes using an algebraic approach to Hough transforms. *Pattern Recognit.* **2018**, *73*, 111–130. [CrossRef]
33. Zhou, H.-L.; Fu, D.-Z.; Dong, J.-J.; Zhang, P.; Chen, D.-X.; Cai, X.-L.; Li, F.-L.; Zhang, X.-L. Orbital angular momentum complex spectrum analyzer for vortex light based on the rotational Doppler effect. *Light Sci. Appl.* **2017**, *6*, e16251. [CrossRef] [PubMed]
34. Flamm, D.; Schulze, C.; Naidoo, D.; Schröter, S.; Forbes, A.; Duparré, M. All-digital holographic tool for mode excitation and analysis in optical fibers. *J. Lightwave Technol.* **2013**, *31*, 1023–2032. [CrossRef]
35. Andersen, J.M.; Alperin, S.N.; Voitiv, A.A.; Holtzmann, W.G.; Gopinath, J.T.; Siemens, M.E. Characterizing vortex beams from a spatial light modulator with collinear phase-shifting holography. *Appl. Opt.* **2019**, *58*, 404–409. [CrossRef] [PubMed]

36. Pinnell, J.; Nape, I.; Sephton, B.; Cox, M.A.; Rodríguez-Fajardo, V.; Forbes, A. Modal analysis of structured light with spatial light modulators: A practical tutorial. *J. Opt. Soc. Am. A* **2020**, *37*, C146–C160. [CrossRef] [PubMed]
37. Leach, J.; Keen, S.; Padgett, M.J.; Saunter, C.; Love, G.D. Direct measurement of the skew angle of the Poynting vector in a helically phased beam. *Opt. Express* **2006**, *14*, 11919–11924. [CrossRef] [PubMed]
38. Bowman, R.W.; Wright, A.J.; Padgett, M.J. An SLM-based Shack–Hartmann wavefront sensor for aberration correction in optical tweezers. *J. Opt.* **2010**, *12*, 124004. [CrossRef]
39. Grunwald, R.; Elsaesser, T.; Bock, M. Spatio-temporal coherence mapping of few-cycle vortex pulses. *Sci. Rep.* **2014**, *4*, 07148. [CrossRef] [PubMed]
40. Zhu, J.; Wu, Y.; Zhou, H.; Zhao, S. Measuring the orbital momentum complex spectrum of light with the Fast Fourier Transform. *Phys. Rev. Appl.* **2023**, *20*, 014010. [CrossRef]
41. D'Errico, A.; D'Amelio, R.; Piccirillo, B.; Cardano, F.; Marrucci, L. Measuring the complex orbital angular momentum spectrum and spatial mode decomposition of structured light beams. *Optica* **2017**, *4*, 1350–1357. [CrossRef]
42. Lin, Z.; Hu, J.; Chen, Y.; Brès, C.-S.; Yu, S. Single-shot Kramers–Kronig complex orbital angular momentum spectrum retrieval. *Adv. Photonics* **2023**, *5*, 036006. [CrossRef]
43. Bazhenov, V.Y.; Soskin, M.S.; Vasnetsov, M.V. Screw Dislocations in Light wavefronts. *J. Mod. Opt.* **1992**, *39*, 985–990. [CrossRef]
44. Soskin, M.S.; Gorshkov, V.N.; Vasnetsov, M.V.; Malos, J.T.; Heckenberg, N.R. Topological charge and angular momentum of light beams carrying optical vortices. *Phys. Rev. A* **1997**, *56*, 4064–40075. [CrossRef]
45. Emile, O.; Emile, J.; Brousseau, C. Detection of the orbital angular momentum in optics. *HAL Open Sci.* **2019**, hal-02162140.
46. Senthilkumaran, P.; Masajada, J.; Sato, S. Interferometry with vortices. *Int. J. Opt.* **2011**, *2012*, 517591. [CrossRef]
47. Liebmann, M.; Treffer, A.; Bock, M.; Seiler, T.; Jahns, J.; Elsaesser, T.; Grunwald, R. Spectral meta-moments reveal hidden signatures of vortex pulses. In *EPJ Web of Conferences 205, 01005 (2019), Proceedings of the XXI International Conference on Ultrafast Phenomena 2018 (UP 2018), Hamburg, Germany, 15–20 July 2018*; EDP Sciences: Les Ulis, France, 2019. [CrossRef]
48. Bryngdahl, O. Geometrical transformations in optics. *J. Opt. Soc. Am.* **1974**, *64*, 1092–1099. [CrossRef]
49. Grunwald, R.; Bock, M. Needle beams: A review. *Adv. Phys. X* **2020**, *5*, 1736950. [CrossRef]
50. Otte, E.; Bobkova, V.; Trinschek, S.; Rosales-Guzmán, C.; Denz, C. Single-shot all-digital approach for measuring the orbital angular momentum spectrum of light. *APL Photonics* **2022**, *7*, 086105. [CrossRef]
51. Yu, H.; Chen, C.; Hu, X.; Yang, H. An efficient recognition method for orbital angular momentum via adaptive deep ELM. *Sensors* **2023**, *23*, 8737. [CrossRef] [PubMed]
52. Fan, W.-Q.; Gao, F.-L.; Xue, F.-C.; Guo, J.-J.; Xiao, Y.; Gu, Y.-J. Experimental recognition of vortex beams in oceanic turbulence combining the Gerchberg–Saxton algorithm and convolutional neural network. *Appl. Opt.* **2024**, *63*, 982–989. [CrossRef]
53. Li, W.; Liu, Y.; Chen, Y.; Cai, Y.; Korotkova, O.; Wang, F. Fast measurement of coherence–orbital angular momentum matrices of random light beams using off-axis holography and coordinate transformation. *Opt. Lett.* **2024**, *49*, 1173–1176. [CrossRef] [PubMed]
54. Wang, J.; Yang, J.Y.; Fazal, I.M.; Ahmed, N.; Yan, Y.; Huang, H.; Ren, Y.; Yue, Y.; Dolinar, S.; Tur, M.; et al. Terabit free-space data transmission employing orbital angular momentum multiplexing. *Nat. Photonics* **2012**, *6*, 488–496. [CrossRef]
55. Torres, J. Multiplexing twisted light. *Nat. Photonics* **2012**, *6*, 420–422. [CrossRef]
56. Santana-Carrillo, R.; Velázquez Peto, J.M.; Sun, G.-H.; Dong, S.-H. Quantum information entropy for a hyperbolic double well potential in the fractional Schrödinger equation. *Entropy* **2023**, *25*, 988. [CrossRef] [PubMed]
57. Solaimani, M.; Dong, S.-H. Quantum information entropies of multiple quantum well systems in fractional Schrödinger equations. *Int. J. Quant. Chem.* **2020**, *120*, e26113. [CrossRef]
58. Solyanik-Gorgone, M.; Ye, J.; Miscuglio, M.; Afanasev, A.; Willner, A.E.; Sorger, V.J. Quantifying information via Shannon entropy in spatially structured optical beams. *Research* **2021**, *1*, 9780760. [CrossRef] [PubMed]